Journal of Geophysical Research: Atmospheres

RESEARCH ARTICLE
10.1029/2017JD028088

Atmospheric Conditions for Advection-Radiation Fog Over the Western Yellow Sea

Liu Yang[1], Jing-Wu Liu[1], Zhao-Peng Ren[2], Shang-Ping Xie[3,1], Su-Ping Zhang[1], and Shan-Hong Gao[1]

[1]Physical Oceanography Laboratory, Qingdao Collaborative Innovation Center of Marine Science and Technology, and Ocean–Atmosphere Interaction and Climate Laboratory, Ocean University of China, Qingdao, China, [2]Qingdao Meteorological Bureau, Qingdao Engineering Technology Research Center for Meteorological Disaster Prevention, Qingdao, China, [3]Scripps Institution of Oceanography, University of California, San Diego, La Jolla, CA, USA

Key Points:
- The air temperature of advection fog frequently drops below SST over the western Yellow Sea
- Sea fog with negative air-sea temperature difference prefers stronger sinking motion and sharper inversion
- Longwave radiative cooling at fog top decreases the surface air temperature through vertical mixing within boundary layer

Correspondence to:
J.-W. Liu,
liujingwu@126.com;
liujingwu@ouc.edu.cn

Citation:
Yang, L., Liu, J.-W., Ren, Z.-P., Xie, S.-P., Zhang, S.-P., & Gao, S.-H. (2018). Atmospheric conditions for advection-radiation fog over the western Yellow Sea. *Journal of Geophysical Research: Atmospheres*, *123*, 5455–5468. https://doi.org/10.1029/2017JD028088

Received 19 NOV 2017
Accepted 29 APR 2018
Accepted article online 6 MAY 2018
Published online 23 MAY 2018

Abstract Advection fog occurs usually when warm and moist air flows over cold sea surface. It is occasionally reported that the fog air temperature falls below sea surface temperature (called here the sea fog with sea surface heating [ssH]) due to longwave radiation cooling at fog top. Using 8-year buoy observations, this study reveals that about 33% of the time, the advection fog is with ssH in the western Yellow Sea. By synthesizing long-term observations from meteorological stations, atmospheric soundings, and offshore buoys, this study further investigates the marine atmospheric boundary layer (MABL) structure and atmospheric circulation associated with the ssH sea fog. Composite analysis shows that a local anomalous high pressure favors widespread formation of the ssH sea fog. The subsidence in the high pressure intensifies the thermal and moist stratification between the MABL and free atmosphere through adiabatic warming. The dry air above helps cool the fog layer by enhancing the longwave radiative cooling at the fog top and the vertical mixing beneath, causing air temperature to drop below sea surface temperature. The ratio of sea fog with ssH to total sea fog decreases from spring to summer as the descending motion and MABL stratification both weaken. This study highlights the importance of longwave radiative cooling at the advection fog top and suggests a way to improve sea fog forecast in the Yellow Sea.

1. Introduction

Sea fog refers to the fog that occurs under the oceanic effects (B. Wang, 1985). Low visibility in sea fog may cause losses of lives and properties, which are comparable to those caused by other weather disasters such as hurricanes and tornadoes (Gultepe et al., 2007; Trémant, 1987). However, forecasts of sea fog still suffer from the lack of observations over the open sea, parameterization uncertainties, and coarse vertical resolution in numerical models for representing boundary layer processes (Bergot & Guedalia, 1994; Gao et al., 2007; Pagowski et al., 2004; Y. Wang et al., 2014).

The Yellow Sea is one of the regions with heaviest sea fog in the world oceans. On average, Qingdao (QD) and Chengshantou stations on the Chinese coast of the Yellow Sea experience more than 50 and 80 fog days per year, respectively (Zhang et al., 2009). The fog season of the western Yellow Sea begins in March and April along with the onset of seasonal inversion and southeasterly winds and ends in August concurrent with the shift of the prevailing winds from southerly to easterly (Zhang et al., 2009). About 80–90% fog over the Yellow Sea in spring and summer is advection fog (B. Wang, 1985), which forms when the air from a warmer water surface flows over colder sea surface, resulting in air temperature lower than its dewpoint and fog formation. Thus, the difference between sea air temperature (SAT) and sea surface temperature (SST) during advection fog is typically between 0.5 and 3 °C as the sea surface cools the near-surface air (B. Wang, 1985).

Albeit with the dominance of advection fog, negative SAT − SST within a fog episode is recently reported in the Yellow Sea (Zhang et al., 2012; Zhang & Ren, 2010). Actually, this phenomenon was previously noted in other regions and received some attention. SAT lower than SST was reported during the haar peak over the North Sea (Lamb et al., 1943). Leipper (1948, 1994) observed that SAT dropped below SST after the formation of fog off the U.S. west coast. Findlater et al. (1989) found SAT of advection fog held at a temperature 1–2 °C below SST off the northeastern coast of Scotland.

The classic view thinks that cooling of unsaturated air by relatively cold sea surface causes advection fog and thus fails to explain the above observational fact (B. Wang, 1985). The SAT lower than SST within warm

advection fog means that the downward sensible heat flux reverses and implies other cooling mechanisms at work. Hereafter, the warm advection fog with negative and positive SAT − SST is referred to as sea fog with sea surface heating (ssH) and cooling (ssC), respectively. Some early studies noted that the colder air than sea surface is related to longwave radiative cooling (LRC) at the fog top (e.g., Douglas, 1930; Lamb, 1943; Petterssen, 1938). Findlater et al. (1989) analyzed the heat budgets and found that the fog top cooling is balanced with the latent and sensible heat flux from sea surface after the formation of advection fog. Zhang and Ren (2010) suggested that the LRC at fog top contributes to negative SAT − SST through turbulent mixing in the fog layer. In the simulation of sea fog near the western coast of the Korean Peninsula, Kim and Yum (2012b) noted negative SAT − SST during advection fog (their Figure 8b) that did not appear in corresponding buoy measurements (their Figure 3).

Although the effects of LRC on fog need to be studied in great depth, how LRC affects marine low clouds has been extensively studied. LRC causes condensation and forms negative buoyancy at cloud top, which induces turbulent mixing within the cloud layer and enhances low-level convective instability (Bretherton & Wyant, 1997; Gerber et al., 2005; Guan et al., 1997; Yamaguchi & Randall, 2008). This vertical mixing cools the marine atmospheric boundary layer (MABL), promotes cloud development (Guan et al., 1997; Rogers & Koračin, 1992; Wood, 2012), and causes the lowering of stratus base and forming sea fog off the California coast (Koračin et al., 2001; Lewis et al., 2003). These numerical and observational studies suggest the important role of LRC in marine clouds.

Previous case studies confirmed the existence of the sea fog with ssH. However, suffering from the influence from specific synoptic conditions, case studies cannot determine whether the sea fog with ssH is prevalent over a longer period. If it is prevalent, LRC at fog top plays an important role even in advection fog. The LRC is strongly modulated by synoptic conditions. For example, descending motion enhances the inversion strength through adiabatic heating and intensifies moist stratification between the free atmosphere and fog layer (Koračin et al., 2001; Leipper, 1994; Lewis et al., 2004; Myers & Norris, 2013). And the dry layer over the fog top can further enhance the LRC (Koračin et al., 2001, 2005) and cool the entire fog layer through vertical mixing (Koračin et al., 2001). The strong modulation of LRC at cloud/fog top by local circulation suggests that the sea fog with ssH may favor certain synoptic and MABL conditions. However, case studies typically focus on specific sea fog events and fail to isolate general features of sea fog with ssH.

The present study uses 8-year observations to compare the synoptic conditions and MABL structures between sea fog with ssH and that with ssC. For the first time, we show the prevalence of sea fog with ssH during the advection fog season in the western Yellow Sea. Composite analysis suggests that sea fog with ssH shares distinct features in MABL and synoptic circulation conditions from the ssC and prefers stronger LRC effect over the fog top. The results suggest that the LRC effect sometimes overcomes the cooling effect of the cold sea surface during the advection fog in the Yellow Sea. This finding advances our knowledge of advection fog in the ocean and potentially promotes the skill of sea fog forecast with numerical models.

Following section 1, section 2 describes the data sets. Section 3 analyzes the boundary layer characteristics for sea fog with ssH. Section 4 investigates the atmospheric circulation corresponding to sea fog with ssH. Section 5 discusses the changes of sea fog with ssH from spring to summer. Section 6 gives conclusions.

2. Data

We use a suite of observations from surface stations, soundings, reanalysis, and buoys to examine the synoptic condition and MABL structure corresponding to sea fog with ssH. Our focus is on spring and summer (March to July) 2008–2015 when advection fog is prevalent and the above data sets are available.

2.1. Surface Station Observations

To investigate the occurrence of sea fog, we use surface observations recorded every 3 hr provided by the China Meteorological Administration. Following Bari et al. (2016), fog is identified when synoptic message indicates fog with visibility lower than 1 km. A fog day is defined as the day when fog is reported at least once (Koračin & Dorman, 2017). Zhang et al. (2009) used QD surface observations (Figure 1) to study the seasonal variations of the Yellow Sea fog. Accordingly, we generally use the observations near QD to represent the state of the western Yellow Sea. Although radiation fog over land is not excluded in this study, it is not a severe problem because of the sea fog's predominance near springtime and summertime QD (shown

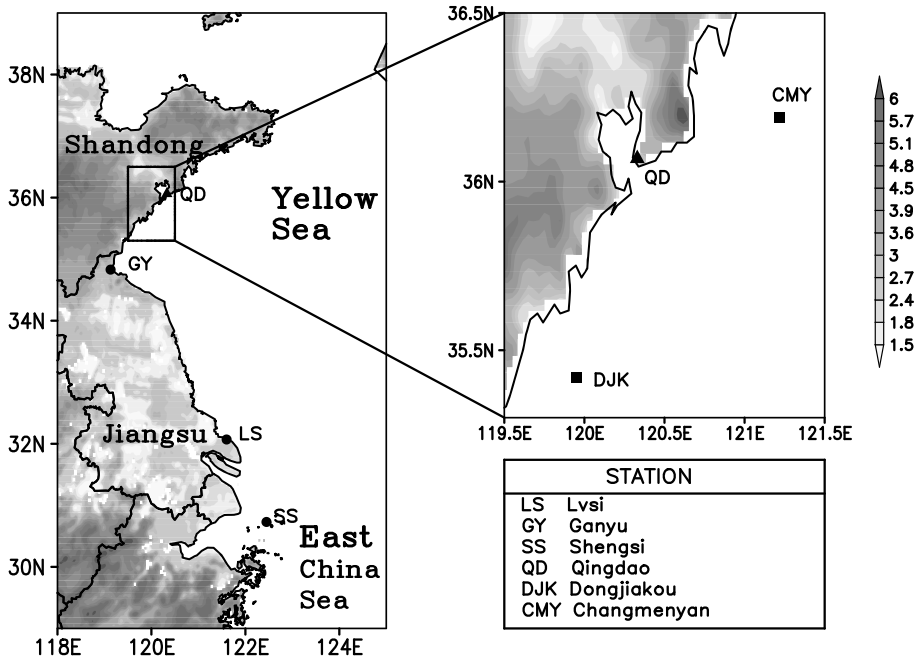

Figure 1. The locations of QD (closed triangle), GY, LS and SS stations (closed circles), and buoys (closed squares). Gray shading represents topography (km) over land. QD = Qingdao; GY = Ganyu; LS = Lvsi; SS = Shengsi; DJK = Dongjiakou; CMY = Changmenyan.

later). In addition, we also use observations from Ganyu (GY), Lvsi (LS), and Shengsi (SS) stations on the western coast of the Yellow and East China Seas to examine fog coverage (Figure 1).

2.2. Soundings

Soundings of Government Furnished Equipment (GFE) (L)-band radar available at 0000 and 1200 UTC at QD are used to study the vertical structures of boundary layer for sea fog. L-band secondary wind radar and The Global Telecommunication System1 (GTS1) digital radiosonde are a new generation of sounding equipment operated by the Chinese Meteorological Bureau recently. We use QD soundings on a 50 m vertical grid to represent the MABL conditions over the northwestern Yellow Sea. QD station is about 1.1 km from the coast and 75 m above the sea surface.

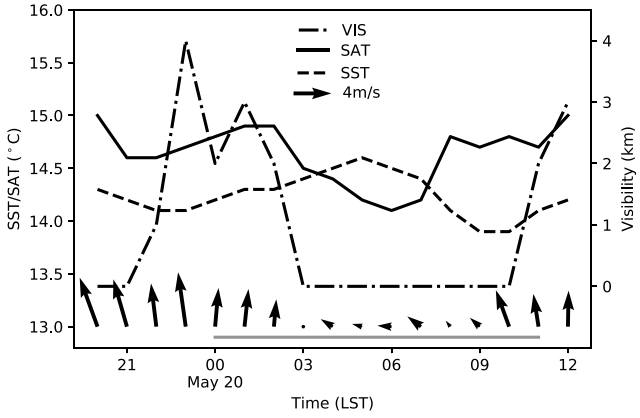

Figure 2. SAT (solid black line, in °C), SST (dashed line, in °C), visibility (dash-dotted line, in km) and surface wind (vectors, m/s) from CMY buoy during 19–20 May 2014. The horizontal gray line indicates the fog duration reported by QD surface station. The relative humidity is 100% during the plot period. SAT = sea air temperature; SST = sea surface temperature; CMY = Changmenyan; QD = Qingdao.

2.3. Buoy Data and the Definition of Sea Fog With ssH

We employ buoy data at Dongjiakou (DJK) and Changmenyan (CMY) stations off QD coast (Figure 1) to investigate the sea-air interface conditions. The buoys record SST, SAT, sea surface wind, and visibility every hour. Yet the buoy visibility measurement was sometimes in poor condition and could not obtain sufficient data, so we use the instrumentally observed visibility at QD station, which is about 80 km from the two buoys. We compared the visibilities between QD station and the buoys and found that the periods with visibility lower than 1 km are roughly consistent (not shown). The buoy observations are excluded when the values fall outside 6 times the standard deviation within the month centered on 12-hourly running mean. Since CMY and DJK observations are missing in 2008 and 2011, respectively, we use the averaged values of the two buoys when their observations overlap and the values from one buoy when the observations of the other one are missing. The results do not change much when the analysis is based upon one buoy (not shown).

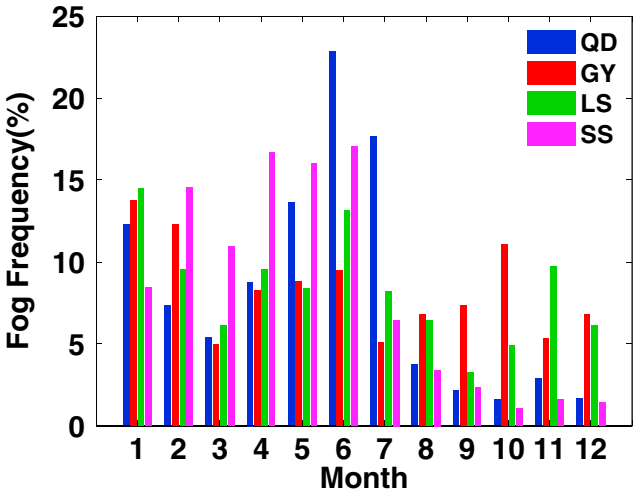

Figure 3. Monthly fog frequencies (%) for QD, GY, LS, and SS. QD = Qingdao; GY = Ganyu; LS = Lvsi; SS = Shengsi.

Sea fog with ssH is recorded when the hourly buoy SAT − SST is negative during fog at QD station. Figure 2 shows the CMY buoy observations and QD visibility for an ssH-fog case on 20 May 2014. A 1-hr episode of ssC fog occurred before 0300 LST on 20 May. After that, SAT dropped below SST with visibility lower than 1 km, forming ssH sea fog. SAT − SST restored to positive sign at 0700 LST, while fog still persisted until 1000 LST. It is interesting to note that SAT − SST exhibited salient diurnal variations, indicating that fog air temperature is modified by the combination of LRC and solar radiation effects. Possibly due to the land breeze at night, the onshore wind significantly weakened between 0300 and 0900 LST. During this period, the weak wind might cause meanders of advection from various directions. However, ssH fog persisted between 0300 and 0700 LST, suggesting that weak horizontal advection from different directions within fog patch did not significantly affect ssH fog. In addition, QD station also reported fog between 0000 and 1100 LST on 20 May (the gray line in Figure 2), roughly consistent with the fog duration observed by the CMY buoy, which verifies the combination of the observations from coastal QD station and nearby offshore buoys.

Kim and Yum (2010, 2012a) used positive SAT − SST before local fog onset to define so-called "cold sea fog," which is actually equivalent to advection fog. By contrast, we focus on the phenomenon of negative SAT − SST during advection fog episodes. So we define ssH fog using hourly buoy SAT − SST during sea fog. We compared the results based upon the time-averaged values during the fog episodes and fog days and found that the outcomes were very close (as will be shown in section 3.2).

2.4. Reanalysis

To examine the atmospheric circulations for sea fog, we use European Centre for Medium-Range Weather Forecasts (ECMWF) Re-Analysis (ERA)-Interim reanalysis provided by the ECMWF (Dee et al., 2011). ERA-Interim fields are on a 0.75° × 0.75° grid with 16 levels below 500 hPa. The spatial resolution is high enough to depict the large-scale atmosphere circulations and characterize its forcing on the MABL. We composite the ERA-Interim fields at 0000 and 1200 UTC concurrent with the soundings at QD.

2.5. Clouds and the Earth's Radiant Energy System

To discuss the effects of higher clouds on sea fog, we use 3-hourly averaged Synoptic Radiative Fluxes and Clouds product from the Clouds and the Earth's Radiant Energy System (CERES) on a 0.1°× 0.1° grid (Carman et al., 1992). We mainly use the upward longwave radiative flux at the top of atmosphere.

2.6. Sea Surface Temperature

We use daily real-time high-resolution global SST on a 0.083° × 0.083° grid from National Centers for Environmental Prediction to examine the relative wind direction to SST gradient (Thiébaux et al., 2003).

3. Boundary Layer Structure for Sea Fog With ssH

3.1. Seasonal Variation

Fog along the western coast of the Yellow Sea exhibits strong seasonal variation (B. Wang, 1985). Figure 3 shows the monthly fog frequency based on observations from coastal meteorological stations. The fog frequency at QD reaches its peak in June and January, respectively. The advection fog dominates in warm season when southeasterly winds prevail and advect moist and warm air to the cold sea surface (Gao et al., 2007; Zhang et al., 2009). The QD fog in winter is generally radiation fog. Similarly, L. Wang et al. (2005) suggested that radiation fog over China inland reaches maximum in winter. The seasonal variations of GY and LS fog resemble QD fog, suggesting a consistent seasonal variation of sea fog along the western coast of the Yellow Sea. Fog frequency at SS reaches its peak in April (pink bars in Figure 3), 2 months earlier than that in QD, suggesting a seasonal northward match of sea fog (B. Wang, 1985).

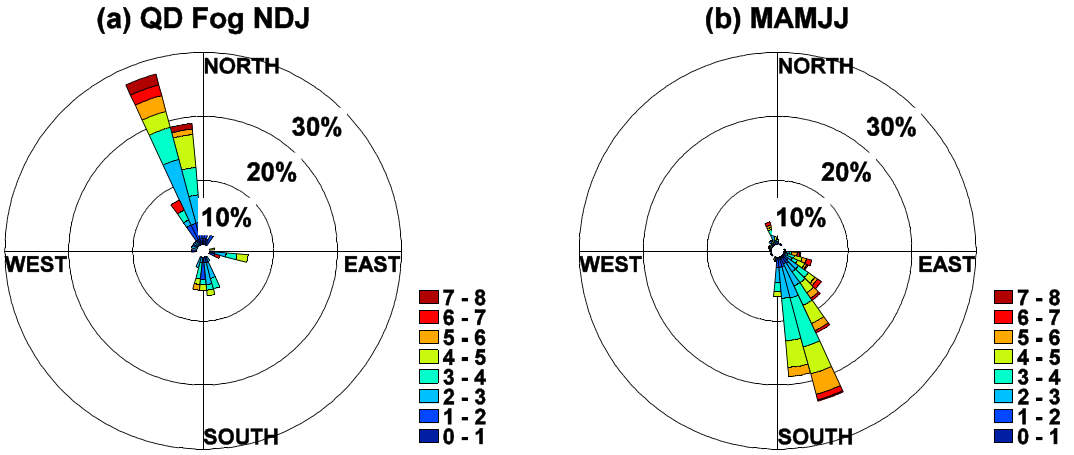

Figure 4. Surface wind rose diagrams (%) based on buoy observations during QD fog: (a) winter (November–January); (b) spring and summer (March–July). Color shade represents wind speed (m/s). QD = Qingdao.

To illustrate seasonal change in formation mechanisms for QD fog, we show the surface wind rose diagrams for fog in cold and warm seasons, respectively (Figure 4). Southeasterly winds prevail during the fog in spring and summer and advect warm and moist air from the warm water to the cold, resulting in advection fog (B. Wang, 1985). By contrast, the winds for the winter fog are generally northwesterly, suggesting that the fog air comes from inland, where radiation fog is prevalent in winter (L. Wang et al., 2005). This distinction in wind directions gives us confidence in the dominance of warm advection fog in spring and summer for QD. We primarily focus on the fog during March to July, accounting for ~ 70% of the annual mean.

3.2. The Frequency of Sea Fog With ssH

To obtain frequency of sea fog with ssH, our analysis includes 216 fog days during March–July in 2008–2015. The probability density functions (PDFs) of hourly SST − SAT concurrent with QD fog show that more than half of SAT − SST are between 0 and 2 °C (black bars in Figure 5), consistent with classical sense of advection fog (Koračin & Dorman, 2017; B. Wang, 1985). However, negative SAT − SST during fog is also frequent (~ 33.4%). We further use averaged SAT − SST values during fog events and fog days. A fog event is defined as continuous fog days. About 21.8% and 17.9% sea fog are with negative SAT − SAT for fog events and days, respectively. These results support the frequent occurrence of sea fog with ssH over the western Yellow Sea.

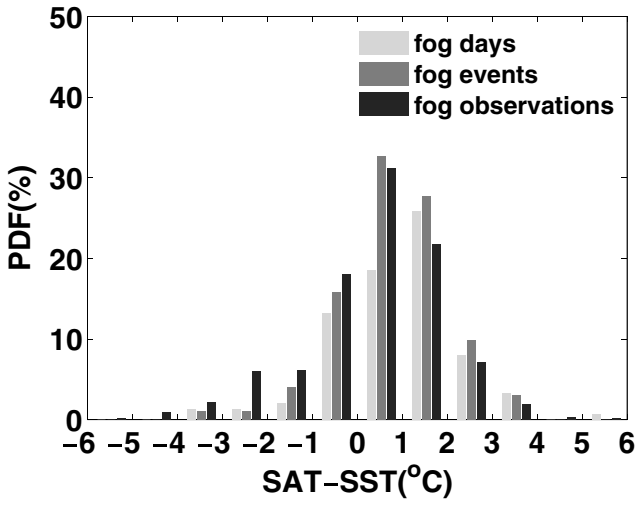

Figure 5. Probability density functions (%) of SAT − SST (°C) for QD fog during March–July. The calculation is based upon averaged SAT − SST during fog days (light gray bars) and fog events (dark gray), and hourly SAT − SST concurrent with QD fog (black). PDF = probability density functions; SAT = sea air temperature; SST = sea surface temperature; QD = Qingdao.

Local SAT − SST is effected by the relationship between the direction of surface wind related to SST gradient, so we compare the PDFs of the so-called SST advection ($-V_{sfc} \cdot \nabla SST$) for sea fog with ssH and ssC (Figure 6c), where V_{sfc} denotes 2-m wind vectors from ERA-Interim and ∇SST is SST gradient. Figure 6c shows that the frequency of positive $-V_{sfc} \cdot \nabla SST$ is ~ 71% for sea fog with ssH, just a little lower than that for ssC (~ 75%). This suggests that surface wind blows from warm to cold sea surface even for the sea fog with ssH, consistent with the dominance of advection fog.

Although warm SST advection prevails, different processes lead to ssH and ssC sea fog. Figure 7 shows the changes in SAT and specific humidity associated with onset of ssH or ssC fog. The timing of the ssH (ssC) fog onset (t_1) is the time when negative (positive) SAT − SST is first observed during a fog event. Following Kim and Yum (2010, 2012a, 2012b), t_0 is 3 hr before t_1. Most sea fog with ssH forms associated with decreases in temperature and specific humidity (lines in Figures 7a and 7b), suggesting that local temperature

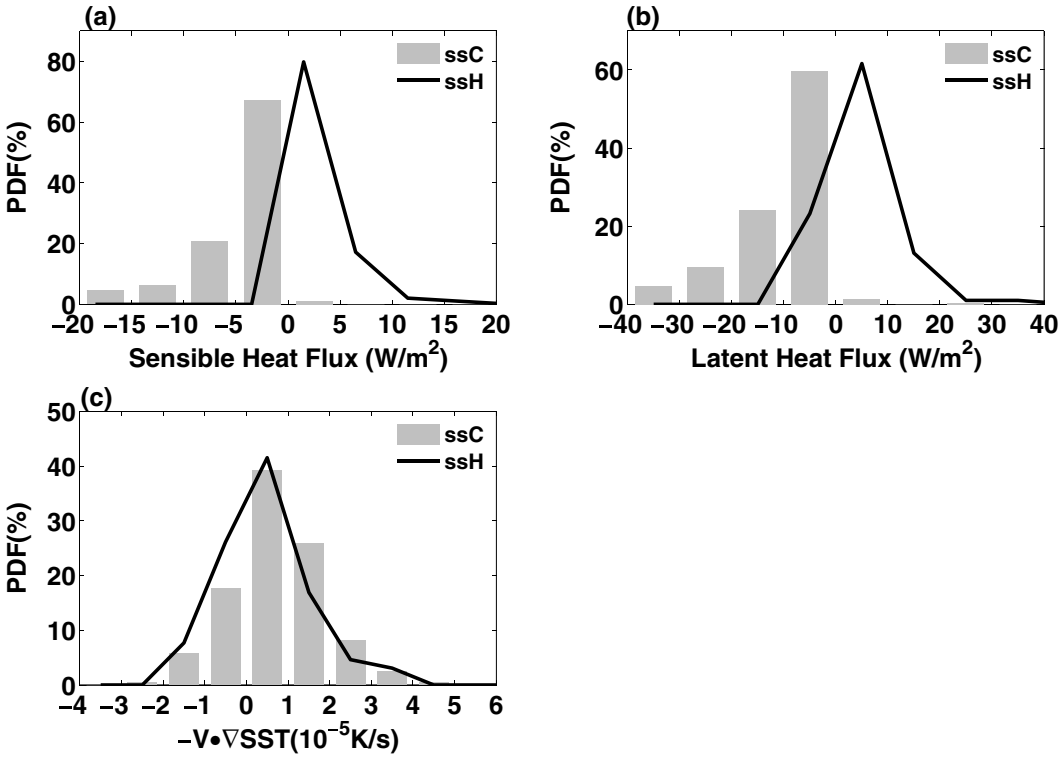

Figure 6. Probability density functions (%) of surface sensible (a; W/m^2) and latent heat fluxes (b; W/m^2) at the buoys and regional averaged $-V_{sfc} \cdot \nabla SST$ (c; 32.25°–38.25°N, 118.5°–124.5°E) obtained from ERA-interim (10^{-5} K/s) for QD fog during March–July. The sensible heat flux and latent heat flux are calculated using $\overline{w'T'} = C_H(SST - SAT)U$ and $\overline{w'q'_s} = C_E(q_s - q)U$. C_H and C_E are 1.0×10^{-3} and 1.2×10^{-3}, respectively, following Smith (1988). PDF = probability density functions; ERA = ECMWF (European Centre for Medium-Range Weather Forecasts) Re-Analysis; QD = Qingdao.

decrease contributes to the ssH fog formation rather than humidity increase. By contrast, the specific humidity increases for more than half of the ssC fog when fog forms (lines in Figure 7b), indicative of the importance of moisture supply for ssC fog. The changes in SAT and specific humidity between ssH and ssC fog are significantly different at 95% confidence level based on a Student's *t* test. The

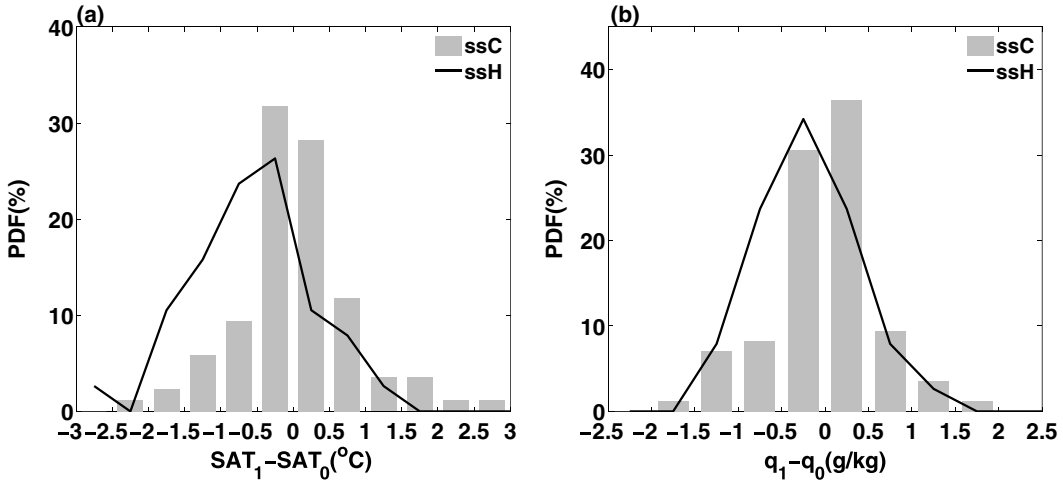

Figure 7. Probability density functions (%) of the changes in buoy temperature (a; °C) and specific humidity (b; g/kg) associated with onsets of ssC (bars) and ssH (lines) sea fog. t_1 is the time when negative (positive) SAT − SST was first observed during a fog event, and t_0 is 3 hr before t_1. PDF = probability density functions; ssC = sea surface cooling; ssH = sea surface heating; SAT = sea air temperature; SST = sea surface temperature.

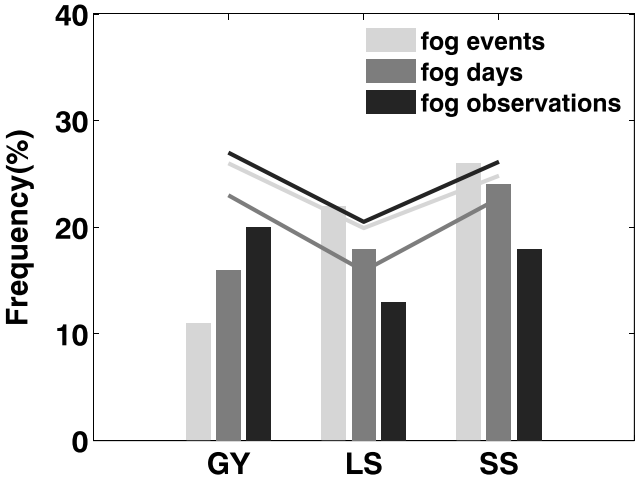

Figure 8. The fog frequencies (lines in %) for GY, LS, and SS stations concurrent with QD fog during March–July. The calculation is based upon averaged SAT − SST during fog days (light gray bars) and fog events (dark gray), and hourly SAT − SST concurrent with QD fog (black). Bars are the frequency differences between sea fog with ssH and ssC corresponding to the above three calculation methods in the same color of the lines. GY = Ganyu; LS = Lvsi; SS = Shengsi; QD = Qingdao; SAT = sea air temperature; SST = sea surface temperature; ssH = sea surface heating; ssC = sea surface cooling.

significance levels are roughly above 90% when slightly altering t_0 and t_1 (not shown), suggesting that the distinction in formation processes is robust for sea fog with ssH and ssC.

After fog formation, sea surface persistently cools sea fog with ssC, while the heat transfers from sea surface to ssH fog (Figure 6a). Thus, the directions of surface latent heat flux are opposite for sea fog with ssH and ssC. The upward surface moisture flux indicates that local moisture supply from the sea surface may also contribute to the development of ssH fog. Thus, the differences in surface fluxes for sea fog with ssH and ssC suggest different processes maintaining the fog air saturation.

In addition, we found that ssH sea fog exhibits more wide spread than ssC. The lines in Figure 8 show the fog frequencies for GY, LS, and SS stations on the western coast of the Yellow Sea concurrent with QD sea fog. The fog frequencies for the three stations are around 25% when QD observed sea fog (black line in Figure 8), indicative of widespread nature of sea fog. All three stations reported more fog concurrent with QD fog with ssH than that with ssC (black bar in Figure 8), suggesting that the sea fog with ssH usually covers a broader area. The results based on fog days and events (bars in dark and light gray in Figure 8) are roughly consistent with the results based on the simultaneous observations concurrent with QD fog. Thus, for simplicity, this study composites the data (soundings, reanalysis, CERES, etc.) at 0000 and 1200 UTC when QD station reported fog in following analysis.

3.3. Boundary Layer Structures

Temperature inversions usually cap sea fog and exert a strong influence on the fog development (Gao et al., 2007; Zhang et al., 2009). Following Cao et al. (2007), we identify the inversions between 75 and 2,000 m within fog soundings at QD. Only 20 of the total 241 soundings without inversions are excluded in our analysis, and the inversions touching the surface are omitted. If two or more inversions are present within a sounding, the inversion with largest increase in potential temperature is selected. The inversion strength is

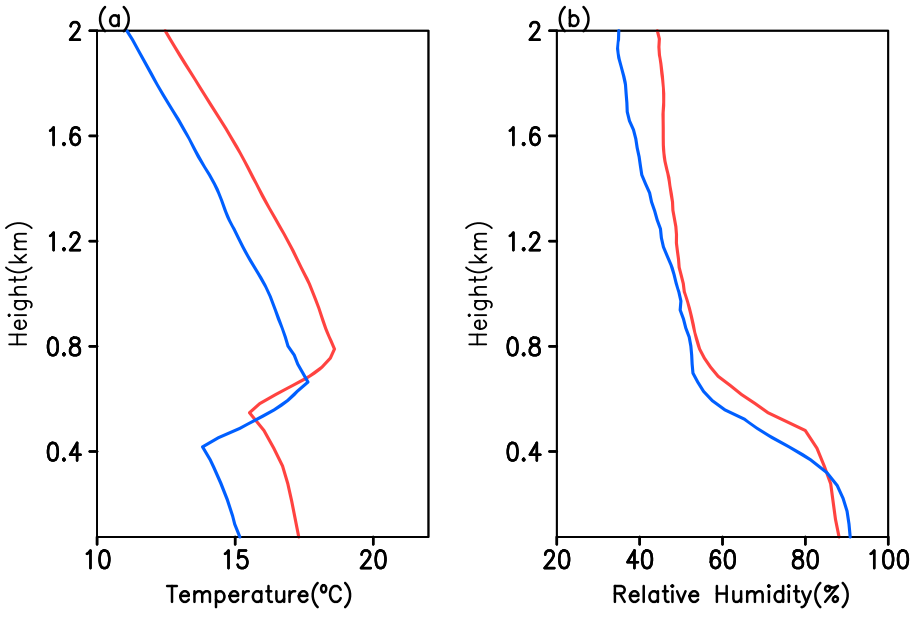

Figure 9. Composite soundings concurrent with QD fog with ssC (red line) and ssH (blue line) during March–July: Temperature (a; °C) and relative humidity (b; %). QD = Qingdao; ssC = sea surface cooling; ssH = sea surface heating.

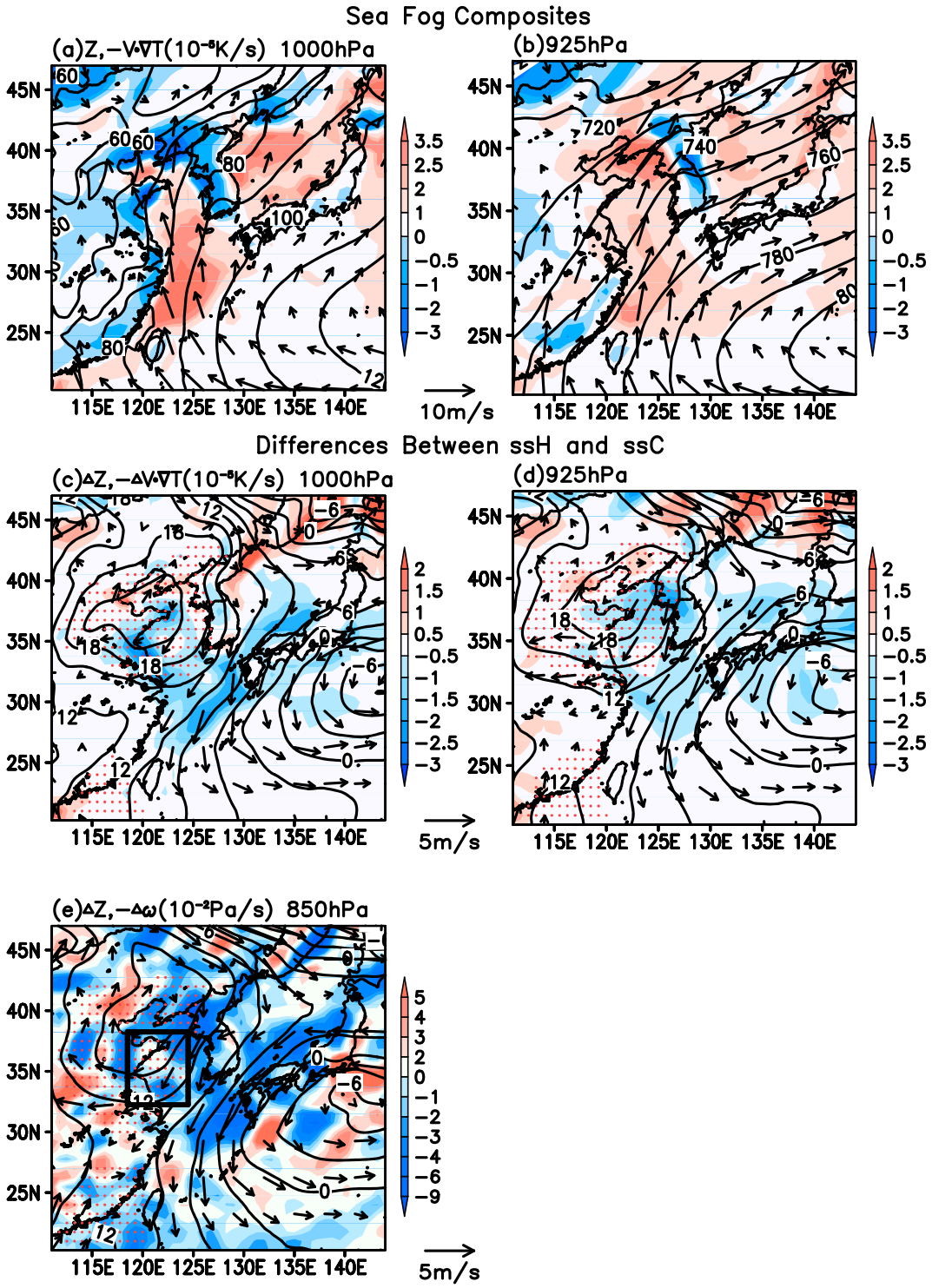

Figure 10. (a) Horizontal wind (vectors, in m/s), temperature advection (shading, in 10^{-5} K/s), and geopotential height (contour, in gpm) at 1,000 hPa for QD fog composite. (b) Same as (a) but for 925 hPa. (c and d) Same as (a) and (b) but for the differences between QD fog with ssH and ssC. (e) Composite differences between QD fog with ssH and ssC: Geopotential height (contour, in gpm), upward motion (shading, in 10^{-2} Pa/s), and horizontal wind (vectors, in m/s). The red dots denote that the geopotential height difference between sea fog with ssH and ssC is significant at the 99.9% confidence level based on a Student's *t* test. QD = Qingdao; ssH = sea surface heating; ssC = sea surface cooling.

defined as the potential temperature difference between inversion top and base (Liu et al., 2016). Following Norris (1998), all soundings between 75 and 2,000 m are divided into three layers (75 m to the inversion base, inversion, and inversion top to 2,000 m), which are normalized by their corresponding average depth. And we rescale the composite soundings of the three layers to their mean depth.

The composite soundings show distinct MABL structures between sea fog with ssH and ssC (Figure 9). For sea fog with ssH, the inversion is found between 417 and 663 m in altitude with an average strength of 6 K, while the inversion for sea fog with ssC is weaker (~ 4.5 K) with higher inversion base (~ 547 m, Figure 9a). Lower inversions trap shallower fog beneath for sea fog with ssH. The relative humidity for sea fog with ssH decreases more sharply upward especially in the inversion and is less than 50% at about 1,500 m in altitude, indicating a much dryer layer above the fog (Figure 9b). Less moisture above the sea fog enhances the outgoing longwave radiation from the fog top, lowering temperature near surface by vertical mixing within the fog.

4. Synoptic Contexts

4.1. Large-Scale Circulation

The differences in MABL are generally related to atmospheric circulation. We calculate the composite large-scale circulation corresponding to QD fog based on ERA-Interim reanalysis (Figures 10a and 10b). Figure 10a shows that the Yellow Sea is located on the northwestern flank of a surface high pressure, where southeasterly winds bring moist and warm air causing sea fog at QD. The southeasterlies also advect the relatively cold air of sea fog from cold sea surface to the warm continent, forming strong cold advection along the western coast of the Yellow Sea. The coastal cold advection reaches its peak on the southern coast of Shandong Peninsula and weakens southward along the coast of Jiangsu Province. The spatial distribution of the cold advection along the western coast of the Yellow Sea during QD fog is consistent with occurrence of fog among the coastal stations (lines in Figure 8). Zhang et al. (2009) suggested that the fog season onset over the Yellow Sea in spring is associated with seasonal inversion produced by the climatological warm advection at 925 hPa. Following Zhang et al. (2009), we examine the composite temperature advection and geopotential height at 925 hPa during QD fog (Figure 10b). The south southwesterly winds in the western Yellow Sea are consistent with the results of Zhang et al. (2009).

To highlight the synoptic conditions corresponding to sea fog with ssH, we calculate the differences in large-scale circulation between sea fog with ssH and ssC (Figures 10c–10e). Figures 10c and 10d depict the differences of temperature advection, wind, and geopotential height between sea fog with ssH and ssC at 1,000 and 925 hPa, respectively. Given that the sea fog events are independent, we use the number of fog events as the degree(s) of freedom. At 1,000 hPa, there is a significant abnormal high pressure to the northwestern Yellow Sea and over Shandong Province (Figure 10c). The related abnormal northeasterlies weaken the warm surface advection over the Yellow Sea and strengthen the cold advection along the coast, especially along the Jiangsu coast, which supports more widespread sea fog with ssH. The warm temperature advection near inversion at 925 hPa is weaker for sea fog with ssH (Figure 10d). This cannot explain the stronger inversion over the sea fog with ssH (Figure 9a), suggesting another factor playing a role.

We thus turn to the vertical motion above MABL (shading in Figure 10e). Compared with sea fog with ssC, stronger sinking motion caused by the abnormal high pressure almost covers the entire Yellow Sea at 850 hPa for sea fog with ssH (Figure 10e). Subsidence can strengthen and lower the inversion (Myers & Norris, 2013), consistent the MABL features for the sea fog with ssH (Figure 9). The warmer and dryer air overlying the MABL produced by adiabatic heating enhances the LRC effect above the MABL (Koračin et al., 2005).

Figures 11a and 11b show the temperature advection and vertical motion averaged over the western Yellow Sea (black box in Figure 10e) for sea fog with ssH and ssC, respectively. The warm advection below 900 hPa is significantly stronger for sea fog with ssC than that for ssH (Figure 11a). Zhang et al. (2009) suggested that the offshore warm advection near 975 hPa contributes to the seasonal inversion in the western Yellow Sea. But our results of sea fog composite show that the warm advection is not the primary cause of inversion variation. On the other hand, the vertical motion is both downward for sea fog with ssH and ssC below 850 hPa but much stronger for ssH. Above 850 hPa, in contrast to the ssC, the strong downward motion for the sea fog with ssH is about 2×10^{-2} Pa/s and reaches 500 hPa (Figure 11b). Strong descending motion above the

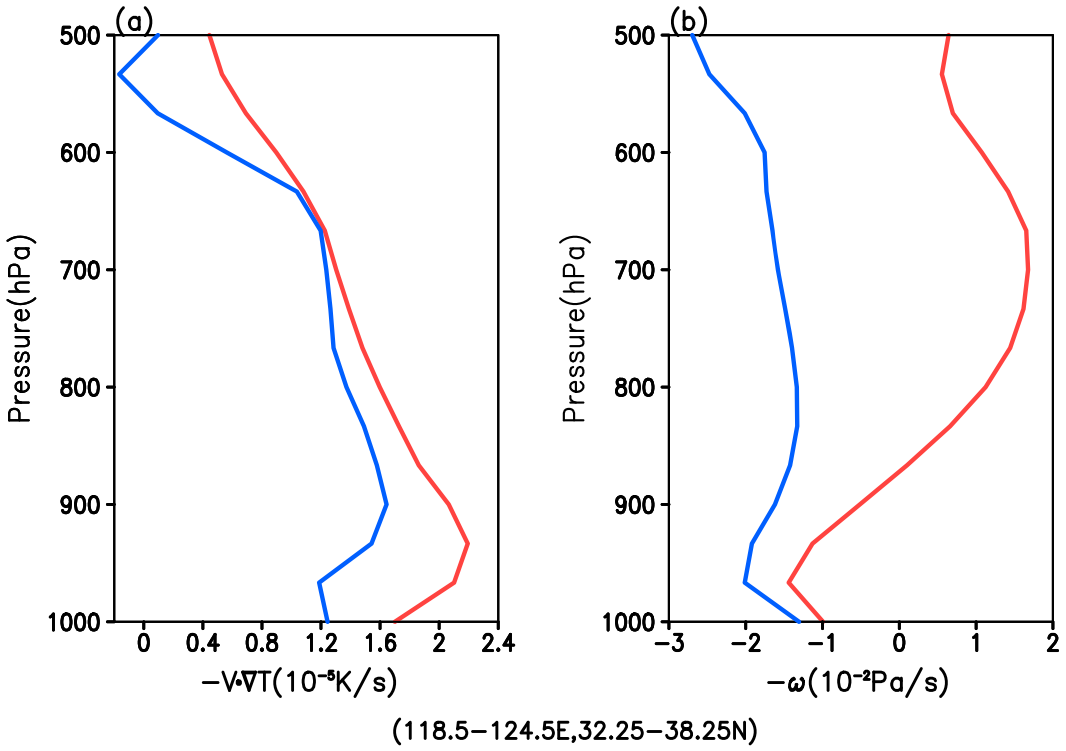

Figure 11. Regional (32.25°–38.25°N, 118.5°–124.5°E) averaged temperature advection (a; 10^{-5} K/s) and upward motion (b; 10^{-2} Pa/s) for QD fog with ssC (red line) and ssH (blue line) during March–July. The observations over land are excluded. QD = Qingdao; ssC = sea surface cooling; ssH = sea surface heating.

MABL reduces the amount of higher clouds due to the subsidence warming and helps intensify the LRC effect through decreasing the downward longwave radiative flux over fog top (Christensen et al., 2013).

Figure 12 shows the PDFs of upward longwave radiative fluxes at top of atmosphere over the western Yellow Sea concurrent with the sea fog with ssH and ssC, respectively. For sea fog with ssH, about half of the upward longwave radiative fluxes are more than 240 W/m^2, which exceeds the 90% percentile for ssC. The higher values of upward longwave radiative fluxes for sea fog with ssH suggest that more longwave radiation comes from lower level of the atmosphere, indicative of less moisture and lower frequency of higher clouds above fog.

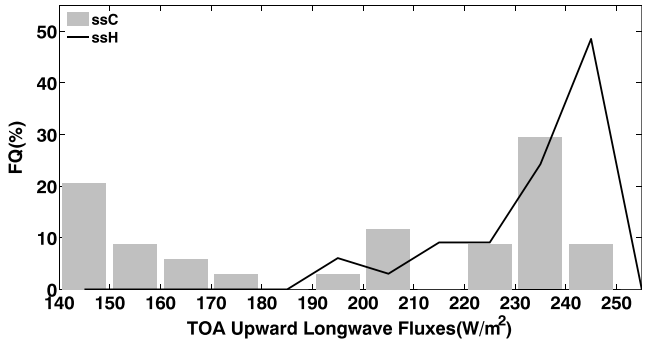

Figure 12. Probability density functions (%) of upward longwave radiation flux (W/m^2) at the top of atmosphere for QD fog with ssC (bars) and ssH (line) during March–July. The observations over land are excluded. QD = Qingdao; ssC = sea surface cooling; ssH = sea surface heating.

4.2. Effects of Vertical Motion

The direct effects of vertical motion on the boundary layer structure and sea fog can be expressed by the following equation (Stull, 1988):

$$\frac{dz_i}{dt} = w_e + w_i, \tag{1}$$

where w_e is the entrainment velocity, z_i boundary layer height, and w_i the vertical velocity at the top of the boundary layer (negative for subsidence). w_i and w_e are roughly in balance when boundary layer height varies slowly with time. w_i is related to the mass-weighted divergence within the boundary layer,

$$w_i = -z_i\{\nabla \cdot V\}, \tag{2}$$

where V is horizontal winds. The descent forces the horizontal divergence within the MABL and tends to decrease the boundary layer thickness and enlarge the horizontal extent covered by the boundary layer. Thus, the abnormal descent and the stronger LRC effect

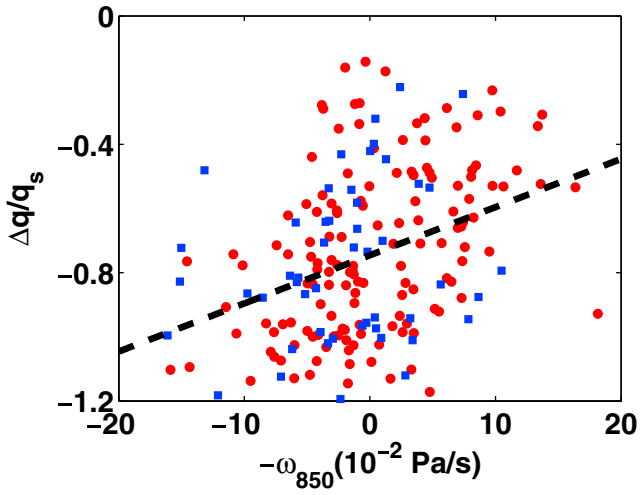

Figure 13. Scatterplots of upward motion (in 10^{-2} Pa/s) and humidity stratification for QD fog with ssH (blue squares) and ssC (red filled circles) during March–July. The humidity stratification is the differences in averaged specific humidity between fog layer and 2–3 km that is normalized by the surface saturation specific humidity. Dotted line indicates simple linear regression line. QD = Qingdao; ssH = sea surface heating; ssC = sea surface cooling.

corresponding to the sea fog with ssH (Figure 10e) increase the entrainment over the MABL top and force horizontal extension of fog patches.

On the other hand, the vertical motion also affects the moist stratification. Figure 13 shows scatters of upward motion and moist stratification ($\Delta q/q_s$) for QD fog with ssH and ssC, respectively. Δq is specific humidity difference between 2 and 3 km and the averaged value of the fog layer (the lower MABL with relative humidity larger than 90%). Then, Δq is normalized by the surface saturation specific humidity q_s to eliminate the influence of ambient temperature following Norris (1998). The scatterplot clearly shows a linear relationship between the descending motion and moist stratification. A 0.01 Pa/s increase of downward motion is related to a 0.15 increase in moist stratification. The stronger moist stratification also intensifies the LRC effect (Figure 12).

5. Spring-to-Summer Changes

The ambient MABL in the western Yellow Sea varies significantly with season (Zhang et al., 2009). Accordingly, sea fog MABL changes substantially from spring to summer. Figure 14 shows the composite soundings for spring and summer sea fog. The averaged inversion strength for sea fog decreases from 7.9 K in spring to 5.5 K in summer (Figure 14a), consistent with the weakening of the moist stratification (Figure 14b). The MABL height defined as the inversion base increases from spring (~ 450 m) to summer (~ 624 m). This is consistent with the case study of Zhang et al. (2012), which suggests that the fog layer in summer is much deeper than that in spring. The changes in fog boundary layer structure indicate seasonal changes in sea fog with ssH. Indeed, the occurrence ratio of sea fog with ssH to total sea fog decreases from spring (~ 34%) to summer (~ 20%, not shown).

The seasonal changes in large-scale circulation for sea fog also help explain the variation in fog boundary layer structure (Figure 15). The downward motion at 850 hPa is much stronger in spring than in summer. This again supports the strong modulation of sea fog by the descent above the boundary layer. We also calculate the composite soundings with respect to vertical motion at 850 hPa and find relatively stronger

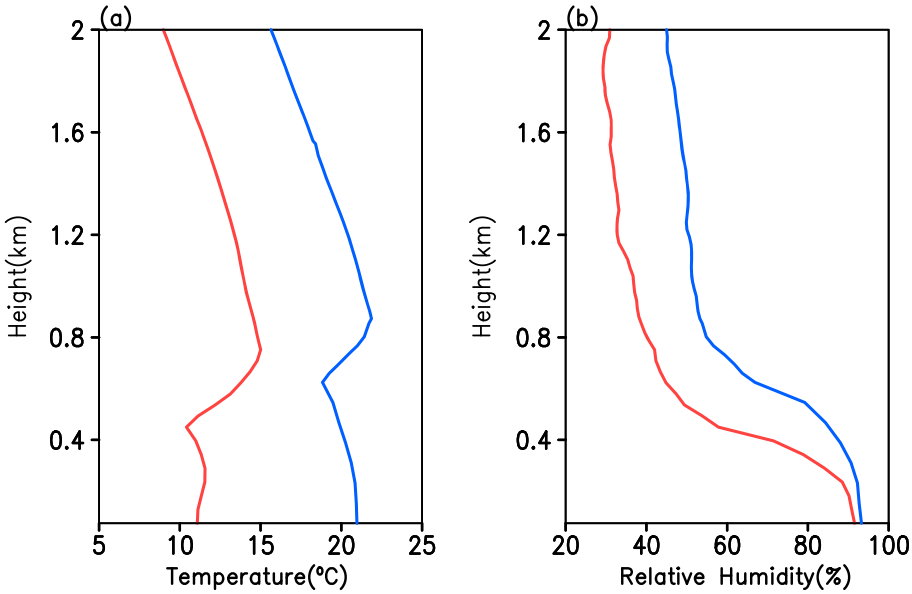

Figure 14. The same as Figure 7 but for MAM (red line) and JJ (blue line), respectively. MAM = March–May; JJ = June–July.

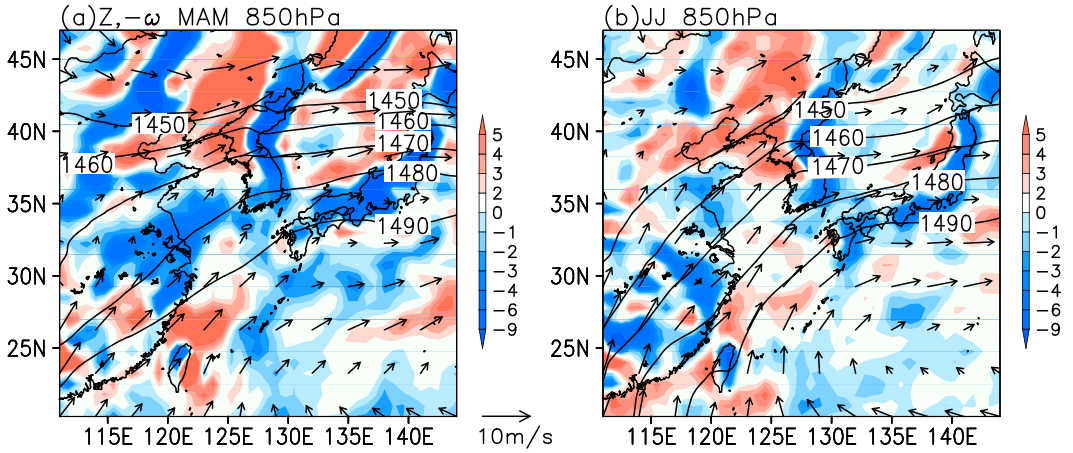

Figure 15. Composite winds (vectors, m/s), vertical motion (shading, -10^{-2} Pa/s) and geopotential height (contours, gpm) at 850 hPa for MAM (a) and JJ (b) QD fog. MAM = March–May; JJ = June–July.

inversion and shallower boundary layer for the descending regime (not shown). But the MABL distinction between the ascending and descending regimes is weaker than that between spring and summer, suggesting that other factors (e.g., seasonal changes in ambient moist and temperature stratifications) are also important.

The downward motion for sea fog in spring is possibly associated with the seasonal surface anticyclone over the Yellow and East China Seas. Zhang et al. (2011) found that this shallow anticyclone is produced by the thermal contrast between the cold sea surface over the central Yellow and East China Seas, surrounding warm land surface, and the warm Kuroshio water. Liu et al. (2016) also showed that the downdraft branch of the secondary circulation induced by the Kuroshio SST front covers cold water of the Yellow and East China Seas. Thus, the small-scale air-sea interaction over the Kuroshio SST front and land-sea thermal contrast potentially exert influence on features of sea fog (e.g., boundary layer structure, fog patch, and SAT − SAT) over the western Yellow Sea.

6. Summary and Discussions

Advection fog prevails under the southeasterly winds in spring and summer over the Yellow Sea. It was previously noted that the fog air temperature occasionally dropped even below SST. But it is still not clear how frequent the negative SAT − SST is during advection fog. To our knowledge, this study first reveals the prevalent occurrences of sea fog with negative SAT − SST and suggests a strong modulation of fog air temperature by LRC effect from fog top. We further use a suite of observations and reanalysis to examine the synoptic contexts for sea fog with ssH and ssC over the Yellow Sea. Composite analysis reveals that local atmospheric circulation and MABL structure for the sea fog with ssH are systematically distinct from those for ssC.

About 33% of the sea fog near QD is with ssH according to offshore buoy observations. Compared with ssC, sea fog with ssH is capped by stronger and lower inversion (Figure 9a) and exhibits larger fog patch (Figure 8). A local abnormal high pressure corresponding to the sea fog with ssH produces stronger descend above and within MABL. The downward motion above 850 hPa strengthens the capping inversion and moist stratification, and the deep descent decreases moisture above the sea fog with ssH through adiabatic heating. Dryer air over the fog intensifies the LRC effect at the fog top.

The decreased occurrence of sea fog with ssH from spring to summer is also related to the sinking motion above fog. The downward motion above the inversion partially contributes to the seasonal decreasing in inversion strength and boundary layer depth associated with QD sea fog. The springtime downward motion over the Yellow Sea is probably induced by a seasonal shallow anticyclone, which is related to the thermal contrast between the cold water of the Yellow Sea and warmer ambient (Zhang et al., 2011).

The variations of fog depth might also play a role. Stronger subsidence produces shallower MABL by pushing the inversion downward (Stull, 1988) and presumably shoals fog layer. The surface air of shallower fog is more

sensitive to the fog top LRC due to smaller thermal inertia of the shorter air volume between the surface and fog top. This effect might be true when comparing fog events (Zhang et al., 2012) but does not hold within a particular fog episode. This is because that the fog top LRC comes into play after fog formation and sometimes causes negative SAT − SAT later on when the fog becomes much deeper (Kim & Yum, 2012b). In other words, negative SAT − SST usually occurs at the mature phase of a sea fog episode when the fog depth is typically greater than the one at fog onset.

Our study highlights the importance of radiative cooling at fog top for sustaining sea fog and indicates a markedly different mechanism for the fog development with the presence of higher clouds. Sea fog without clouds above can be retrieved using satellite observations (Yi et al., 2015; Zhang & Yi, 2013), while the ability of detecting fog in the cloudy area is rather poor. Thus, features of sea fog based upon the satellite retrievals might introduce some uncertainties from this conditional sampling.

A recent study found that the skill in simulating sea fog is strongly sensitive to the vertical resolution near fog top (S. Gao, personal communication, March 21, 2018) and suggests a positive feedback between LRC at fog top and liquid water content within the fog. Their finding supports the importance of the LRC effect for advection fog, and therefore the models with better representation of radiative processes may show better skills in sea fog forecasts. Our study isolates tropospheric and boundary layer conditions that favor sea fog with air temperature colder than SST and indicates that fog top LRC probably plays a more important role under stronger subsidence. To shed light on the corresponding boundary processes of sea fog with ssH, quantitative assessment using boundary models with higher vertical resolution is desirable.

Acknowledgments
This work is supported by the Natural Science Foundation of China (NSFC; 41505003 and 41490640) and Natural Science Foundation of Shandong Province (2014ZRE29087). S. -P. Zhang and S. -H. Gao were supported by NSFC (41576108) and NSFC (41276009), respectively. The authors wish to thank N. Zhang for his valuable comments. The data in this study are obtained from the ECMWF data server (ERA-Interim, https://www.ecmwf.int/), the National Centers for Environmental Prediction (SST, http://polar.ncep.noaa.gov/sst/ophi/), and the NASA Langley Research Center Atmospheric Sciences Data Center (CERES, https://ceres.larc.nasa.gov/).

References

Bari, D., Bergot, T., & Khlifi, M. E. (2016). Local meteorological and large scale weather characteristics of fog over the Grand Casablanca region, Morocco. *Journal of Applied Meteorology and Climatology*, *55*(8), 1731–1745. https://doi.org/10.1175/JAMC-D-15-0314.1

Bergot, T., & Guedalia, D. (1994). Numerical forecasting of radiation fog. Part I: Numerical model and sensitivity tests. *Monthly Weather Review*, *122*(6), 1218–1230. https://doi.org/10.1175/1520-0493(1994)122%3C1218:NFORFP%3E2.0.CO;2

Bretherton, C. S., & Wyant, M. C. (1997). Moisture transport, lower-tropospheric stability, and decoupling of cloud-topped boundary layers. *Journal of the Atmospheric Sciences*, *54*(1), 148–167. https://doi.org/10.1175/1520-0469(1997)054%3C0148:MTLTSA%3E2.0.CO;2

Cao, G. X., Giambelluca, T. W., Stevens, D. E., & Schroeder, T. A. (2007). Inversion variability in the Hawaiian trade wind regime. *Journal of Climate*, *27*, 4421–4432.

Carman, S. L., Cooper, J. E., Miller, J., Harrison, E. F., & Barkstrom, B. R. (1992). Clouds and the Earth's Radiant Energy System (CERES). *Bulletin of the American Meteorological Society*, *77*(5), 853–868.

Christensen, M. W., Carri, G. G., Stephens, G. L., & Cotton, W. R. (2013). Radiative impacts of free-tropospheric clouds on the properties of marine stratocumulus. *Journal of the Atmospheric Sciences*, *70*(10), 3102–3118. https://doi.org/10.1175/JAS-D-12-0287.1

Dee, D. P., Uppala, S. M., Simmons, A. J., Berrisford, P., Poli, P., Kobayashi, S., et al. (2011). The ERA-Interim reanalysis: Configuration and performance of the data assimilation system. *Quarterly Journal of the Royal Meteorological Society*, *137*(656), 553–597. https://doi.org/10.1002/qj.828

Douglas, C. (1930). Cold fogs over the sea. *Meteorological Magazine*, *65*, 133–135.

Findlater, J., Roach, W., & McHugh, B. (1989). The haar of north-east Scotland. *Quarterly Journal of the Royal Meteorological Society*, *115*(487), 581–608. https://doi.org/10.1002/qj.49711548709

Gao, S. H., Lin, X., Shen, B., & Fu, G. (2007). A heavy sea fog event over the Yellow Sea in March 2005: Analysis and numerical modeling. *Advances in Atmospheric Sciences*, *24*(1), 65–81. https://doi.org/10.1007/s00376-007-0065-2

Gerber, H., Frick, G., Malinowski, S. P., Brenguier, J. L., & Burnet, F. (2005). Holes and entrainment in stratocumulus. *Journal of the Atmospheric Sciences*, *62*(2), 443–459. https://doi.org/10.1175/JAS-3399.1

Guan, H., Yau, M. K., & Davies, R. (1997). The effects of longwave radiation in a small cumulus cloud. *Journal of the Atmospheric Sciences*, *54*(17), 2201–2214. https://doi.org/10.1175/1520-0469(1997)054%3C2201:TEOLRI%3E2.0.CO;2

Gultepe, I., Tardif, R., Michaelides, S. C., Cermak, J., Bott, A., Bendix, J., et al. (2007). Fog research: A review of past achievements and future perspectives. *Pure and Applied Geophysics*, *164*(6-7), 1121–1159. https://doi.org/10.1007/s00024-007-0211-x

Kim, C. K., & Yum, S. S. (2010). Local meteorological and synoptic characteristics of fogs formed over Incheon International Airport in the west coast of Korea. *Advances in Atmospheric Sciences*, *27*(4), 761–776. https://doi.org/10.1007/s00376-009-9090-7

Kim, C. K., & Yum, S. S. (2012a). Marine boundary layer structure for the sea fog formation off the west coast of the Korean Peninsula. *Pure and Applied Geophysics*, *169*(5–6), 1121–1135. https://doi.org/10.1007/s00024-011-0325-z

Kim, C. K., & Yum, S. S. (2012b). A numerical study of sea-fog formation over cold sea surface using a one-dimensional turbulence model coupled with the weather research and forecasting model. *Boundary-Layer Meteorology*, *143*(3), 481–505. https://doi.org/10.1007/s10546-012-9706-9

Koračin, D., & Dorman, C. E. (Eds.) (2017). *Marine fog: Challenges and advancements in observations, modeling, and forecasting* (pp. 291–343). Zurich: Springer International Publishing.

Koračin, D., Leipper, D. F., & Lewis, J. M. (2005). Modeling sea fog on the U. S. California coast during a hot spell event. *Geofizika*, *22*(1), 59–82.

Koračin, D., Lewis, J., Thompson, W. T., Dorman, C. E., & Businger, J. A. (2001). Transition of stratus into fog along the California coast: Observations and modeling. *Journal of the Atmospheric Sciences*, *58*(13), 1714–1731. https://doi.org/10.1175/1520-0469(2001)058%3C1714:TOSIFA%3E2.0.CO;2

Lamb, H. (1943). Haars or North Sea fogs on the coasts of Great Britain. Meteorology Office Publication M. O. 504, 24 pp.

Leipper, D. F. (1948). Fog development at San Diego, California. *Journal of Marine Research*, *7*, 337–346.

Leipper, D. F. (1994). Fog on the U. S. West Coast, a review. *Bulletin of the American Meteorological Society*, *72*, 229–240.

Lewis, J. M., Koračin, D., Rabin, R., & Businger, J. (2003). Sea fog off the California coast: Viewed in the context of transient weather systems. *Journal of Geophysical Research*, *108*(D15), 4457. https://doi.org/10.1029/2002JD002833

Lewis, J. M., Koračin, D., & Redmond, K. T. (2004). Sea fog research in the United Kingdom and United States: A historical essay including outlook. *Bulletin of the American Meteorological Society*, *85*(3), 395–408. https://doi.org/10.1175/BAMS-85-3-395

Liu, J. W., Xie, S. P., Yang, S., & Zhang, S. P. (2016). Low-cloud transitions across the Kuroshio front in the East China Sea. *Journal of Climate*, *29*(12), 4429–4443.

Myers, T. A., & Norris, J. R. (2013). Observational evidence that enhanced subsidence reduces subtropical marine boundary layer cloudiness. *Journal of Climate*, *26*(19), 7507–7524. https://doi.org/10.1175/JCLI-D-12-00736.1

Norris, J. R. (1998). Low cloud type over the ocean from surface observations. Part I: Relationship to surface meteorology and the vertical distribution of temperature and moisture. *Journal of Climate*, *11*(3), 369–382. https://doi.org/10.1175/1520-0442(1998)011%3C0369:LCTOTO%3E2.0.CO;2

Pagowski, M., Gultepe, I., & King, P. (2004). Analysis and modeling of an extremely dense fog event in southern Ontario. *Journal of Applied Meteorology and Climatology*, *43*(1), 3–16. https://doi.org/10.1175/1520-0450(2004)043%3C0003:AAMOAE%3E2.0.CO;2

Petterssen, S. (1938). On the causes and the forecasting of the California fog. *Bulletin of the American Meteorological Society*, *19*(2), 49–55.

Rogers, D. P., & Koračin, D. (1992). Radiative transfer and turbulence in the cloud-topped marine atmospheric boundary layer. *Journal of the Atmospheric Sciences*, *49*(16), 1473–1486. https://doi.org/10.1175/1520-0469(1992)049%3C1473:RTATIT%3E2.0.CO;2

Smith, S. D. (1988). Coefficients for sea surface wind speed stress, heat flux, and wind profiles as a function of wind speed and temperature. *Journal of Geophysical Research*, *93*(C12), 15,467–15,471. https://doi.org/10.1029/JC093iC12p15467

Stull, R. B. (1988). An introduction to boundary layer meteorology. Atmospheric Sciences Library, 399 pp.

Thiébaux, J., Rogers, E., Wang, W., & Katz, B. (2003). A new higher-solution blended real-time global sea surface temperature analysis. *Bulletin of the American Meteorological Society*, *84*(5), 645–656. https://doi.org/10.1175/BAMS-84-5-645

Trémant, M. (1987). La prévision du brouillard en mer. Météorologie Maritimeet Activities. Oceanograpiques Connexes Raport, WMO, 20, 127.

Wang, B. H. (1985). *Sea fog* (p. 2). Beijing: China Ocean Press.

Wang, L. P., Chen, S., & Dong, A. (2005). The distribution and seasonal variations of fog in China (in Chinese). *Acta Geographica Sinica*, *60*, 689–697.

Wang, Y., Gao, S. H., Fu, G., Sun, J. L., & Zhang, S. P. (2014). Assimilating MTSAT-derived humidity in nowcasting sea fog over the Yellow Sea. *Weather Forecasting*, *29*(2), 205–225. https://doi.org/10.1175/WAF-D-12-00123.1

Wood, R. (2012). Stratocumulus clouds. *Monthly Weather Review*, *140*(8), 2373–2423. https://doi.org/10.1175/MWR-D-11-00121.1

Yamaguchi, T., & Randall, D. A. (2008). Large-eddy simulation of evaporatively driven entrainment in cloud-topped mixed layers. *Journal of the Atmospheric Sciences*, *65*(5), 1481–1504. https://doi.org/10.1175/2007JAS2438.1

Yi, L., Zhang, S. P., Thies, B., Shi, X. M., Trachte, K., & Bendix, J. (2015). Spatio-temporal detection of fog and low stratus top heights over the Yellow Sea with geostationary satellite data as a precondition for ground fog detection—A feasibility study. *Atmospheric Research*, *151*, 212–223. https://doi.org/10.1016/j.atmosres.2014.03.020

Zhang, S. P., Li, M., Meng, X. G., Fu, G., Ren, Z. P., & Gao, S. H. (2012). A comparison study between spring and summer fogs in the Yellow Sea—Observations and mechanisms. *Pure and Applied Geophysics*, *169*(5-6), 1001–1017. https://doi.org/10.1007/s00024-011-0358-3

Zhang, S. P., Liu, J. W., Xie, S. P., & Meng, X. G. (2011). The formation of a surface anticyclone over the Yellow and East China Seas in spring. *Journal of the Meteorological Society of Japan*, *89*(2), 119–131. https://doi.org/10.2151/jmsj.2011-202

Zhang, S. P., & Ren, Z. P. (2010). The influence of thermal effects of underlaying surface on the spring sea fog over the Yellow Sea—Observations and numerical simulation (in Chinese). *Acta Meteorologica Sinica*, *68*, 116–125.

Zhang, S. P., Xie, S. P., Liu, Q. Y., Yang, Y. Q., Wang, X. G., & Ren, Z. P. (2009). Seasonal variations of Yellow Sea fog: Observations and mechanisms. *Journal of Climate*, *22*(24), 6758–6772. https://doi.org/10.1175/2009JCLI2806.1

Zhang, S. P., & Yi, L. (2013). A comprehensive dynamic threshold algorithm for daytime sea fog retrieval over the Chinese adjacent seas. *Pure and Applied Geophysics*, *170*(11), 1931–1944. https://doi.org/10.1007/s00024-013-0641-6